THE JOURNAL OF PHYSICAL CHEMISTRY C
A JOURNAL OF THE AMERICAN CHEMICAL SOCIETY

pubs.acs.org/JPCC

Article

Interface Alloying Design to Improve the Dispersion of TiB_2 Nanoparticles in Al Composites: A First-Principles Study

Qian Wang, Yuanyuan Li, Siyi Chen, Xiaomin Liu, Zhe Chen, Mingliang Wang,* Hong Zhu,* and Haowei Wang

Cite This: *J. Phys. Chem. C* 2021, 125, 5937−5946

Read Online

ACCESS | Metrics & More | Article Recommendations | Supporting Information

ABSTRACT: An extensive first-principles database of alloying behavior of 37 elements in the Al(111)/TiB_2(0001) interface is presented. The interfacial ability is systematically compared via the formation energy, interface energy, and work of adhesion. The thermodynamically most stable interface with the Ti terminal and center stacking sequence is selected to analyze the alloying behavior. According to the interfacial stability and wettability, an alloying trend map containing 11 excellent elements (Mg, Ca, Ag, Ce, Au, Pd, Y, Sc, Pt, Hf, and Zr) is obtained. These elements can effectively improve the dispersion of TiB_2 particles in Al-based composites by promoting the formation of the Al/TiB_2 interface and improving the interfacial wettability. Based on the number of valence electrons in the d orbital, these alloying elements can be divided into zero-d (Mg and Ca), low-d (Sc, Y, Zr, Ce, and Hf), and high-d (Pd, Ag, Pt, and Au) elements. In combination with the electronic structure of the alloying interfaces, the alloying mechanisms are discussed depending on the hybridization between Al and alloying atoms. Generally, our calculation guides the interface alloying strategy to enhance the particle dispersion in the metal matrix composite and provides a fundamental explanation for the related interfacial mechanisms.

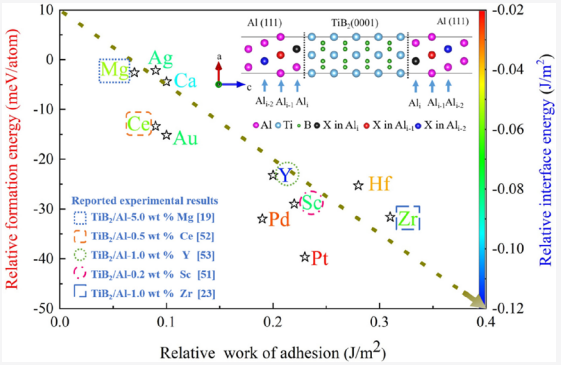

1. INTRODUCTION

Over the past few decades, the TiB_2 particles reinforced Al matrix composites have been widely developed as novel structural materials owing to their superior strength, higher stiffness, and lower thermal expansion coefficient.[1,2] However, due to the poor wettability between the TiB_2 particles and the Al matrix, these particles tend to agglomerate along the grain boundaries or interdendritic regions during the casting process.[3,4] Such particulate clustering has resulted in the reduced ductility of the composite.[5] The decline in ductility can be ascribed to three aspects: (i) the TiB_2 cluster limits the ability of the Al matrix to withstand deformation, leading to crack formation and expansion on the interface,[6,7] (ii) the accumulation of clusters and pores leads to earlier failure,[8] and (iii) the coexistence of TiB_2 clusters and large brittle intermetallic compounds causes stress concentration.[9,10] Therefore, the further development of the TiB_2/Al composite is hindered by the existence of TiB_2 aggregation.

Traditionally, the TiB_2/Al composite is synthesized by the mixing salt reaction method.[11−14] Once the TiB_2/Al composite is cast under the common solidification condition, the as-cast composite is subsequently processed by the traditional deformation processes (i.e., rolling, extruding, or forging) to refine its microstructure.[15−17] In most cases, the TiB_2 clusters in the as-deformed composite are still on the grain boundaries along with the deforming directions. Indeed, the TiB_2 clusters are difficult to separate by the normal deformation method in the as-cast composite made at the lower cooling rate.

To solve this particle aggregation problem, both kinetic and thermodynamic factors should be considered in this Al−TiB_2 system. For the kinetics-based factor, the particle dispersion should be determined by the cooling rate in the solidification. When the composite melt solidifies at a higher cooling rate, the distribution of TiB_2 particles should be more uniform.[18−20] Therefore, some rapid solidification methods have been proposed, such as powder metallurgy,[18] spray codeposition,[21] and melt spinning.[22] Although the degree of the particle agglomeration can be alleviated by these methods, the core problem of TiB_2 clusters (i.e., the poor wettability between the TiB_2 and the Al matrix) needs to be further improved.[19]

Subsequently, the manipulation of the Al/TiB_2 interface by alloying addition as the main thermodynamics method has been widely proposed.[19,23,24] Generally, the alloying atoms are considered to affect the interface characteristics between the particle and matrix and then improve the corresponding

Received: January 14, 2021
Revised: February 22, 2021
Published: March 4, 2021

https://dx.doi.org/10.1021/acs.jpcc.1c00371
J. Phys. Chem. C 2021, 125, 5937−5946

interface ability. Macroscopically, such alternation may improve the wettability between the particle and matrix and then promote particle dispersion (section S1 in the Supporting Information). Nevertheless, there is a lack of theoretical or experimental verifications on this opinion due to the limitation of experimental conditions.

In recent years, the first-principles calculation based on density functional theory (DFT) has been widely applied to study the interface characteristics for the metal−ceramics system.[25,26] In the Al−TiB_2 system, Zhang et al.[27] used the Gibbs absorption isotherm and DFT calculation to clarify the contact angle (θ, 0−180°) between TiB_2 and Al (eq 1)[28] which were mainly determined by the interfacial energy ($\gamma_{Al(S)/TiB_2(S)}$) of the Al(S)/TiB_2(S) interface.

$$\nu_\gamma = \cos\theta = \frac{\gamma_{Al(L)/TiB_2(S)} - \gamma_{Al(S)/TiB_2(S)}}{\gamma_{Al(L)/Al(S)}} \quad (1)$$

Since the interface energies of Al(L)/TiB_2(S) and Al(L)/Al(S) interfaces almost remained constant (i.e., 0.85 and 0.16 J/m^2, respectively), $\gamma_{Al(S)/TiB_2(S)}$ is the only viable option herein. Clearly, a smaller contact angle (θ) is related to an optimum wettability. If $\gamma_{Al(S)/TiB_2(S)}$ is reduced in eq 1, the cos θ value is elevated. Correspondingly, the contact angle (θ) is reduced to signify the better wettability between the TiB_2 and Al matrix.

Notably, it is difficult to compare the variable $\gamma_{Al(S)/TiB_2(S)}$ for the original and alloyed Al(S)/TiB_2(S) interfaces directly, since the calculated interface energy is chemical potential (or synthesis condition) dependent.[29] Therefore, the relative interface energies of the alloyed interface have been widely employed in many related studies. For example, Zhao et al.[30] compared the formation energy and the Griffith work of the original and alloyed (i.e., Re, Mo, Ta, and Cr) Ni/Ni_3Al interfaces to explain the vacancy-mediated alloying strengthening mechanism of Ni-based single crystal superalloy. Phongpreecha et al.[31] theoretically verify the mechanisms of the CuO interlayer enhancing the wetting and adhesion of the Ag/YSZ interface by DFT calculation. Moreover, they employed the work of adhesion as a descriptor to screen some new metal oxides with better wettability. Shin et al.[32] provided a large DFT database, which contained the segregation energies (i.e., relative interface energy) of 34 elements in the Al/Al_2Cu interface. According to the verification of effective elements (i.e., Mn, Zr, and Sc), they provided a large number of useful elements which can enhance the stability of the interface to speed up the alloying tactic of high-temperature Al−Cu alloys.

Referring to the experimental conditions of alloying, the theoretical interfacial stability should be considered before studying the interface alloying. That is to say, the suitable alloying position of various elements in the interface should be tested. Otherwise, the DFT calculation may obtain the opposite result from the experimental observation. For instance, Deng et al. claimed that the Mg hindered the formation of the Al/TiB_2 interface theoretically by DFT calculation.[33] However, Youseff et al.[19] found the Mg addition can promote the formation of the Al/TiB_2 interface experimentally. This difference may be caused by the alloying position. In Deng's research, Mg substituted Al atoms at the interface, which may be inconsistent with experimental observations. Therefore, multiple alloying positions should be compared in alloying interface research.

Based on the above discussion, it is necessary and feasible to make the comprehensive alloying design on the Al/TiB_2 interface characteristics via DFT calculation. Then, some favorable elements can be screened to improve the particle dispersion in the TiB_2/Al composite. Referring to the interface orientation observed in the experiment,[4,34,35] the Al(111)/TiB_2(0001) is the most typical interface identified in this composite. Therefore, the original and alloyed Al(111)/TiB_2(0001) interfaces were compared in the present study. First, the formation energy of the interface was used to estimate the interfacial stability of alloyed interfaces. Second, the interface energy and the work of adhesion were adopted to evaluate the interfacial wettability. As a result, the alloying trend map was obtained to explain available experimental results and guide future experiment design. Finally, the alloying mechanisms were clarified by the analyses on the electronic structure of the alloying interfaces. The main purpose of this work is to provide an alloying strategy to accelerate the improvement of TiB_2 agglomerate in the Al matrix and also illustrate the related interfacial mechanisms herein.

2. COMPUTATIONAL DETAILS

The DFT calculations were performed in the Vienna Ab initio Simulation Package (VASP) with the projected augmented wave (PAW) pseudopotentials and a plane-wave basis set.[36−38] The Perdew−Burke−Ernzerhof (PBE) exchange-correlation functional within the generalized gradient approximation (GGA) was applied. The calculations were performed with a plane-wave cutoff energy of 450 eV, and the self-consistency convergence criterion for energy tolerance was set to 10^{-6} eV/atom. Similarly, the gamma centered 22 × 22 × 22 k-point meshes for the bulk unit cell and 6 × 6 × 1 k-point meshes for the Al(111)/TiB_2(0001) interface supercell were employed, respectively. The valence electrons for the adopted pseudopotentials of Al, B, and Ti atoms were $3s^23p^1$, $2s^22p^1$, and $3s^23p^63d^24s^2$, respectively. The convergence criterion for forces was 0.01 eV/Å during structural relaxation via conjugate gradient minimization. A vacuum layer of 10 Å thickness has been added to the surface supercell to prevent unwanted interactions between the slab and its periodic arrangement. During the structural relaxation, the atomic positions were allowed to freely relax in three directions by fixing volume and cell shape.

3. RESULTS AND DISCUSSION

3.1. Original Al(111)/TiB_2(0001) Interfaces. Initially, the involved bulk phases (i.e., Al ($Fm\bar{3}m$), Ti ($P6_3/mmc$), β-B ($R\bar{3}m$), and TiB_2 ($P6/mmm$) are optimized at the ground state. Each optimized lattice parameter in Table S1 agrees well with the corresponding experimental and theoretical results (section S2 in the Supporting Information). Considering the structural symmetry, a sandwich-like interface supercell model was employed. Based on the convergence test (section S3 in the Supporting Information), two six-layer Al(111) slabs and a nine-layer Ti- or B-terminated TiB_2(0001) slab were used to construct an Al(111)/TiB_2(0001) interface supercell model.

Six different interface models are constructed by considering the terminal (Ti or B) and stacking sequence (i.e., center, top, and bridge). These models are shown in Figure 1, where the locations of Al atoms are different. Taking Ti terminal models as an example, in the center stacking, the interfacial Al atoms are located above the second layer sites of TiB_2(0001) slabs; in

https://dx.doi.org/10.1021/acs.jpcc.1c00371
J. Phys. Chem. C 2021, 125, 5937−5946

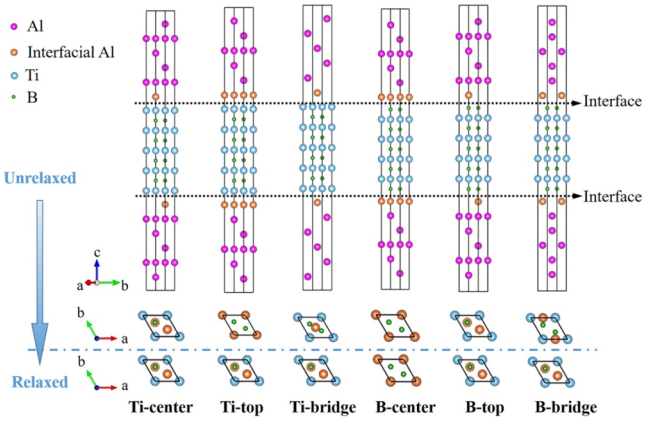

Figure 1. Front view and top view of three stacking sequences of Ti- and B-terminated Al(111)/TiB_2(0001) interface models at both unrelaxed and relaxed states.

top stacking, the interfacial Al atoms are located above the surface Ti atoms of the TiB_2(0001) slab; while in bridge stacking, the interface Al atoms are located above the middle position of the second layer of the TiB_2(0001) slab. According to previous studies,[29,33] the interface distance (d_0) is initially set to 2.20 Å for Ti-terminated models and 2.00 Å for B-terminated models. After relaxation, the relative atom positions of the model are exhibited in Figure 1 and the interface distances are listed in Table 1.

Table 1. Interface Distance (d_0) and the Work of Adhesion (W_{ad}) of Al(111)/TiB_2(0001) Interfaces

		relaxed			
	unrelaxed	d_0 (Å)		W_{ad} (J/m^2)	
terminal-stacking sequence	d_0 (Å)	this work	others[29]	this work	others[29]
Ti-center	2.20	2.21	2.38	3.82	3.17
Ti-top	2.20	2.21	2.23	3.76	3.18
Ti-bridge	2.20	2.19	2.18	3.83	3.18
B-center	2.00	1.64	1.65	3.55	2.77
B-top	2.00	2.07	2.09	3.21	2.43
B-bridge	2.00	2.03	2.09	3.22	2.44

3.1.1. Interfacial Bonding Strength. To investigate their interfacial bonding strength as well as interface stability,[39] the interfacial distance (d_0) and the work of adhesion (W_{ad}) are employed. The work of adhesion (W_{ad}) is defined as the following[40−42]

$$W_{ad} = \frac{1}{2A}(E_{slab}^{Al} + E_{slab}^{TiB_2} - E_{interface}) \quad (2)$$

where E_{slab}^{Al} and $E_{slab}^{TiB_2}$ are the total energies of two six-layer Al(111) surface slabs and a nine-layer TiB_2(0001) surface slab with the same lattice parameters of their relaxed interface models, respectively; $E_{interface}$ is the energy of the interface model after fully relaxed; $2A$ represents the total area of two interface regions in each interface model (i.e., two identical interfaces at the top and bottom of the model).

The interface distance (d_0) and the work of adhesion (W_{ad}) of Al(111)/TiB_2(0001) interfaces are listed in Table 1. For the Ti-terminated interface models, three modules (i.e., Ti-center, Ti-top, and Ti-bridge) show similar values of d_0 and W_{ad}. That is because the relaxed Ti-top and Ti-bridge interfaces changed to the Ti-center interface structure via relaxation (Figure 1). Therefore, the Ti-center interface structure is the most stable one. This conclusion is in good compliance with the reports from both Han et al.[29] and Deng et al.[33] However, for the B-terminated interface models, the three interface modules (i.e., B-center, B-top, and B-bridge) exhibit different values of d_0 and W_{ad}. Among them, the B-center interface structure with the smallest d_0 and the largest W_{ad} (Table 1) is the most stable structure. Besides, the B-top and B-bridge interfaces have the same structure after relaxation, so they exhibit similar values of d_0 and W_{ad} in Table 1.

3.1.2. Interfacial Stability. The interface stability has been further evaluated based on the interface energy from the thermodynamic viewpoint. The interface energy (γ_{int}) is defined as the following[33,43−45]

$$\gamma_{int} = \frac{1}{2A}(E_{interface} - N_{Al}\mu_{Al} - N_{Ti}\mu_{Ti} - N_B\mu_B) \quad (3)$$

where N_{Al}, N_{Ti}, and N_B refer to the number of the corresponding atoms in the interfaces; μ_{Al}, μ_{Ti}, and μ_B are the chemical potentials of Al, Ti, and B, respectively.

Accordingly, the interface energies of Ti-center and B-center Al(111)/TiB_2(0001) interfaces can be plotted as a function of the chemical potential of B in Figure 2 (explained by section S4 in the Supporting Information). As the chemical potential of B increases, the interface energy of the B-center interface decreases and that of the Ti-center interface increases. In detail, the Ti-center interface has a smaller interface energy of ~ −0.26 J/m^2 under the Ti-rich conditions. For the B-rich case, the smaller interfacial energy is assigned to the B-center interface with γ_{int} = 0.97 J/m^2. Over most of the B chemical potential, the Ti-center interface has a smaller interface energy, which is thermodynamically more favorable. Combining with the work of adhesion in Table 1, the Ti-center interface with a larger value shows a higher interfacial bonding strength than the B-center interface. Consequently, the most stable Ti-center interface is used to further study the effects of alloying elements on the interface characteristics.

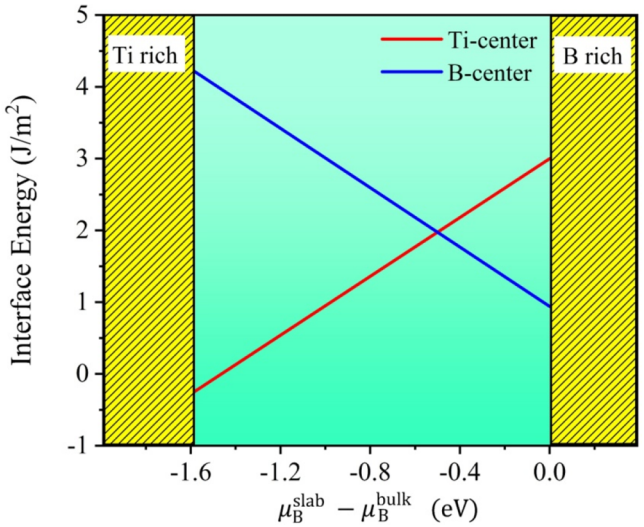

Figure 2. Calculated Al(111)/TiB_2(0001) interfacial energies as a function of the chemical potential of B.

3.2. Alloyed Al(111)/TiB_2(0001) Interfaces. *3.2.1. Interfacial Stability.* The 37 elements, i.e., 7 main group (MG)

https://dx.doi.org/10.1021/acs.jpcc.1c00371
J. Phys. Chem. C 2021, 125, 5937−5946

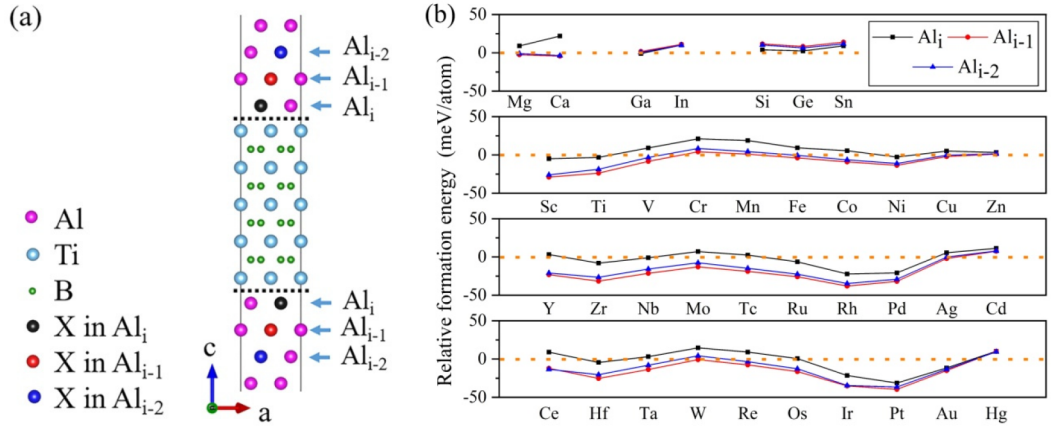

Figure 3. (a) Schematic diagram of atomic substitution sites of alloying elements at a 2 × 2 × 1 Ti-center Al(111)/TiB_2(0001) interface supercell with the 2 at % alloying ratio. (b) Relative formation energies of 37 alloying interfaces. The dotted line represents the original interface.

elements (i.e., Mg, Ca, Ga, In, Si, Ge, and Sn) and 30 transition metal (TM) elements (i.e., 3d-TM, 4d-TM, and 5d-TM), are chosen to explore the alloying behaviors. Only one alloying atom (X) is introduced in each Ti-center Al(111)/TiB_2(0001) interface structure. Meanwhile, three substitution sites (Al_i, Al_{i-1}, Al_{i-2}) from the interface to the bulk region are employed to determine the optimal substitution position of the X atom (Figure 3a). To evaluate the site preference of the alloying atoms and the stability of the alloyed interface, the relative interface formation energy (ΔE_f) was calculated using the following equation[30,46]

$$\Delta E_f = \frac{1}{N_{Total}}[(E^X_{interface} - E_{interface}) - N^X(E^{bulk}_X - E^{bulk}_{Al})] \quad (4)$$

where $E_{interface}$ ($E^X_{interface}$) is the total energy of the original (alloyed) interface supercell; N_{Total} and N_X are the numbers of the total atoms and alloyed atoms in the supercell, respectively; E^{bulk}_{Al} and E^{bulk}_X are the ground state energies of the individual atoms in the corresponding elemental bulk states, respectively; and ΔE_f is the relative formation energy of the alloyed interface. A negative ΔE_f value indicates that the alloyed interface is more stable than the original interface, and a positive value indicates interface instability.

To conduct a comprehensive study of alloying design on the interface, a 2 × 2 × 1 Ti-center Al(111)/TiB_2(0001) interface supercell with an alloying ratio of 2 at. % is adopted based on the convergence tests of alloying ratios (section S5 in the Supporting Information). Since 37 alloying atoms are introduced into the interface supercell, ΔE_f values of alloyed interfaces with atoms located at three substitution sites are calculated and plotted in Figure 3b. The alloying atoms of MG exhibit dissimilar segregation tendencies. For Mg and Ca (group IIA), the ΔE_f values with the alloying elements at three sites follow the sequence of $Al_i > Al_{i-2} > Al_{i-1}$. Both alloying atoms should prefer to segregate at the Al_{i-1} site. For Ga and In (group IIIA), the differences between ΔE_f values of alloying atoms at three substitution sites are smaller than 1 meV/atom, indicating that the segregation behaviors of these alloying atoms are independent of their interfacial location. Judged by the quantitative values, the optimal position for Ga is the Al_i site, and for In, it is the Al_{i-2} site. However, In segregation with a positive ΔE_f value means its unstable alloyed interface structure. For Si, Ge, and Sn (group IVA), all atoms show a similar segregation tendency, and the site preference is given as a sequence of $Al_i > Al_{i-2} > Al_{i-1}$. This tendency is also observed in the semicoherent Al/Al_2Cu interface.[47] Unfortunately, these alloyed interfaces possess entirely positive ΔE_f values, indicating their natural instability.

Similar segregation trends can be observed in the Ti-center Al(111)/TiB_2(0001) interface with the alloyed TM elements. For each element, the alloying atom at the Al_i site has the highest ΔE_f value. Except for Ce and Hg, the ΔE_f values for alloying atoms at the Al_{i-1} site are slightly lower than those at the Al_{i-2} site. Therefore, the optimal substitution positions are Al_{i-2} site for Ce and Hg and Al_{i-1} site for other TM elements. Moreover, as the atomic number of atoms in the same period increases, the variation of ΔE_f for alloying atoms at three substitution sites gradually becomes smaller. That is to say, all TM elements prefer to stay away from the interface (Al_i). A similar phenomenon is also seen in the coherent Al/Al_2Cu interface with 3d-TM elements but not in the semicoherent Al/Al_2Cu interface.[32] This may be caused by a different degree of misfit and interfacial strain, which needs to be further studied. Furthermore, when the alloying atoms are segregated at the optimal position, the Cr, Mn, Zn, Cd, and Hg alloying elements possess positive ΔE_f values, indicating that these alloyed interfaces have inferior stabilities over the original one and should not be considered thereafter.

Consequently, the interfacial stabilities of the Ti-center can be enhanced by 28 elements and the optimal substitution position is mainly the Al_{i-1} site, except for Ga (Al_i site) and Ce (Al_{i-2} site). Therefore, it is more reasonable to compare the interfacial energetic fluctuation when the alloying atoms substitute at their optimal sites.

3.2.2. Interfacial Wettability. According to the contact angle equation (eq 1), if the interface energy of the alloyed Al/TiB_2 interface is lower than that of the original Al/TiB_2 interface, the wettability between Al and TiB_2 can be improved by alloying. Therefore, the dispersion of TiB_2 nanoparticles in Al composites can be improved by the interface alloying. Referring to Figure 2, the interface energy of the Al(111)/TiB_2(0001) interface depends on the chemical potential of B; thus, the relative interface energy ($\Delta\gamma_{int}$) is employed to conveniently estimate the variation of interface energy after alloying, which is defined as follows[32,33,48]

https://dx.doi.org/10.1021/acs.jpcc.1c00371
J. Phys. Chem. C 2021, 125, 5937−5946

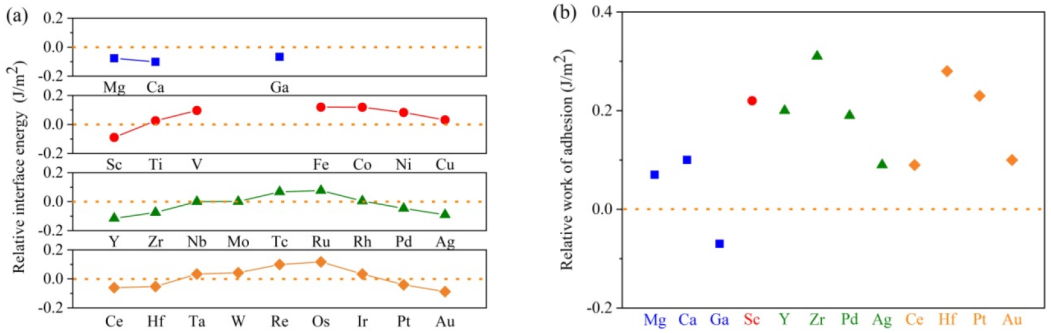

Figure 4. Calculated results of the Ti-center Al(111)/TiB_2(0001) interface with alloying atoms: (a) relative interface energy and (b) relative work of adhesion. The dotted line represents the original interface.

$$\Delta\gamma_{int} = \frac{1}{2A}[(E^{X}_{interface} - E_{interface}) - N^{X}(\mu_{X}^{bulk} - \mu_{Al}^{bulk})] \quad (5)$$

where $\Delta\gamma_{int}$ is the relative interface energy of the alloyed interface. A negative value of $\Delta\gamma_{in}$ indicates that the alloying atoms (X) can enhance the interfacial thermodynamic stability by reducing the interface energy; $E_{interface}$ ($E^{X}_{interface}$) is the total energy of the original (alloyed) interface supercell; and N_X is the number of the alloyed atoms in the supercell. To calculate μ_X^{bulk}, a bulk model with 24 Al atoms is applied and the central Al atom is replaced with an X atom. 2A refers to the interfacial area of two interfaces in the supercell.

The $\Delta\gamma_{int}$ values of alloyed Ti-center Al(111)/TiB_2(0001) interfaces are demonstrated in Figure 4a. Among MG elements, the $\Delta\gamma_{int}$ values are negative for the alloying systems with Mg, Ca, and Ga atoms. These alloying elements can reduce the corresponding interface energies, and the degree of reduction is given as a sequence of Ca > Mg > Ga. It is noteworthy that the current alloying effect of Mg is opposite to the result reported by Deng et al.[33] This may be because, in their calculation, Mg was substituted in the Al_i site, rather than the optimal Al_{i-1} position identified in our present work.

Similarly, for TM elements, the Sc of 3d-TM, Y, Zr, Pd, and Ag of 4d-TM, and Ce, Hf, Pt, and Au of 5d-TM elements can reduce the interface energy of the Al(111)/TiB_2(0001) interface, while others can elevate the interface energy. The identical alloying effect of the Ce element is also reported by Xue et al.[49] Moreover, the variation of $\Delta\gamma_{int}$ values about the atomic number of TM elements in the same period follows a convex-down parabolic-like tendency. An analogous alloying phenomenon also can be seen in the grain boundary of aluminum.[50] Besides, most of the isoelectronic elements in the same group possess similar $\Delta\gamma_{int}$ values, suggesting that the valence electron of alloying atoms shows a great influence on the interface energy.

Overall, three MG elements (i.e., Mg, Ca, and Ga) and nine TM elements (i.e., Sc, Y, Zr, Pd, Ag, Ce, Hf, Pt, and Au) can enhance the interfacial thermodynamic stability due to the reduced interface energies. Combined with eq 1, the wettability of TiB_2 particles and the Al matrix should be increased by adding these alloying elements.

To further verify the role of 12 elements on the interfacial wettability, the work of adhesion (W_{ad}) of corresponding alloyed interfaces was calculated. Based on Young's equation, Saiz et al.[51] found that the interfacial wettability can be evaluated using W_{ad}. As W_{ad} increases, the wettability of the corresponding interface should be improved. Thus, the relative work of adhesion (ΔW_{ad}) is further employed to describe the variation of the interfacial wettability after alloying, which is calculated as follows[33,52]

$$W^{X}_{ad} = \frac{1}{2A}(E^{Al-X}_{slab} + E^{TiB_2}_{slab} - E^{X}_{interface}) \quad (6)$$

$$\Delta W_{ad} = W^{X}_{ad} - W_{ad} \quad (7)$$

where W^{X}_{ad} is the work of adhesion of the alloyed interface and ΔW_{ad} is the relative work of adhesion of the alloyed interface. A positive ΔW_{ad} value means that the alloying atoms can intensify the interfacial bonding strength to enhance wettability.

The relative work of adhesion (ΔW_{ad}) of alloyed Ti-center Al(111)/TiB_2(0001) interfaces is shown in Figure 4b. Referring to the original interface (Table 1), it can be found that, except for Ga, all elements can enhance the work of adhesion of interfaces after alloying. Among them, Zr has the maximum ΔW_{ad} value (~0.31 J/m^2) and Mg has a minimum value of ~0.07 J/m^2. Overall, the interfacial wettability of the Ti-center Al(111)/TiB_2(0001) interface can be enhanced by these 11 alloying elements (i.e., Mg, Ca, Ag, Ce, Au, Pd, Y, Sc, Pt, Hf, and Zr) via reducing interface energy and increasing work of adhesion.

3.3. Alloying Trend Map. To improve the degree of the dispersion of TiB_2 particles in Al matrix composites, alloying addition is a simple and effective method. According to experimental research, several elements have shown the positive alloying effect, such as Mg,[19] Ce,[49] and Sc.[53] Although their influence levels are different, they are difficult to compare due to different experimental environments. Based on the analysis of interface formation energy, interface energy, and work of adhesion, the alloying effect of various elements on the Al/TiB_2 interface can be compared comprehensively. Accordingly, an alloying trend map can be obtained in Figure 5.

After introducing 37 alloy atoms in the Ti-center Al(111)/TiB_2(0001) interface, 11 elements (i.e., Mg, Ca, Ag, Ce, Au, Pd, Y, Sc, Pt, Hf, and Zr) exhibit the obvious alloying effect by synchronously enhancing the interfacial stability and wettability. It means that these elements can effectively improve the dispersion of TiB_2 particles in Al-based composites by promoting the formation of the Al/TiB_2 interface and improving the wettability between Al and TiB_2.

Among them, the alloying effect of Mg in the TiB_2/Al composite is also found by Youssef et al.[19] They found that Mg improved the dispersion of TiB_2 particles in the Al matrix by reducing the critical solidification velocity of composites and argued that the most likely mechanism was that Mg reduced the interfacial energy, leading to better wetting behavior

https://dx.doi.org/10.1021/acs.jpcc.1c00371
J. Phys. Chem. C 2021, 125, 5937−5946

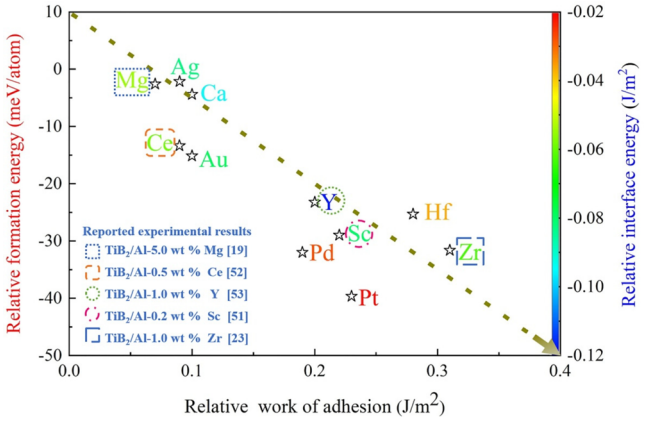

Figure 5. Alloying trend graph of the Ti-center Al(111)/TiB_2(0001) interface with 11 alloying elements.

between the TiB_2 and Al. Herein, our calculated result provides a direct theoretical verification for their experimental results. Similarly, the improvement of Ce on the Al/TiB_2 interface ability agrees with the view of Xue et al.[49] Combining DFT calculation with experiment observation, they found that the absorption of the Ce element on the Al/TiB_2 interface can promote the dispersion of TiB_2 particles via reducing the interfacial energy. Conclusively, Ce should be the proper element for the dispersion of TiB_2 particles.

Notably, the alloying effects of Y, Sc, and Zr are similar, and due to their excellent overall performance, their effects are significantly better than other elements in Figure 5. Moreover, the influence of these elements is consistent with many reports in the literature. For example, Zhang et al.[54] found that the addition of Y massively increased grain bridges and then promoted the grain refinement of the 6 TiB_2/Al-5Cu composite. Sun et al.[53] found that addition of Sc can significantly improve the dispersion of TiB_2 particles in the Al matrix and the degree of particle dispersion increases with the elevated Sc content. Jha et al.[23] found that the distribution of TiB_2 in the Al−Mg−Zr alloy is more dispersed than that in commercial purity Al, and they claimed the Mg addition can promote the formation of a TiB_2/Al interface to a small extent, while the Zr addition can further promote the TiB_2 dispersion effectively. This opinion is consistent with our calculated results in Figure 5; i.e., the alloying effect of Zr is better than that of Mg on the Al/TiB_2 interface. Clearly, the alloying effects of these elements have been confirmed by the reported experimental results, indicating the viability of our strategies on the interfacial calculation.

To facilitate the selection of experiments, the alloying effects of these elements are sorted in detail. First, the order of interface stability depending on the formation energy is Pt > Pd > Zr > Sc > Hf > Y > Au > Ce > Ag > Ca > Mg. Thus, the Pt-alloyed interface is thermodynamically most favorable. Second, the interface wettability based on the interface energy follows the sequence of Y > Ca > Ag > Sc > Au > Mg > Zr > Ce > Hf > Pd > Pt. Hence, from a thermodynamic point of view, the Y-alloyed interface shows the best wettability among all alloying interfaces. Finally, the interface wettability depending on the work of adhesion obeys the order of Zr > Hf > Pt > Sc > Y > Pd > Ca > Au > Ag > Ce > Mg. Therefore, based on the interfacial bonding strength, the Zr-alloyed interface displays the highest wettability.

3.4. Alloying Mechanism. According to the interfacial formation energy, interface energy, and work of adhesion of 37 alloying Ti-center Al(111)/TiB_2(0001) interfaces, 11 elements can simultaneously enhance the interfacial stability and wettability. In detail, they are two main group (MG) elements (i.e., Mg and Ca) and nine transition metal (TM) elements (i.e., Ag, Ce, Au, Pd, Y, Sc, Pt, Hf, and Zr). According to the number of valence electrons in the d orbital, these elements can be further divided into zero-d (i.e., Mg and Ca), low-d (i.e., Sc, Y, Zr, Ce, and Hf), and high-d (i.e., Pd, Ag, Pt, and Au) alloying elements. Based on the Bader population analysis of an alloyed interface (section S5 in the Supporting Information), the alloying mechanism in each series of zero-/low-/high-d alloying elements should be similar, and the alloying mechanisms of these series should be different. To clarify the alloying mechanism, the electron structures of the original and Mg-, Sc-, and Pt-alloyed Ti-center Al(111)/TiB_2(0001) interfaces are calculated and analyzed.

3.4.1. Charge Density Difference. To provide a direct bonding description of atoms at the interface, the charge density difference maps of Ti-center Al(111)/TiB_2(0001) interfaces are calculated as follows[55,56]

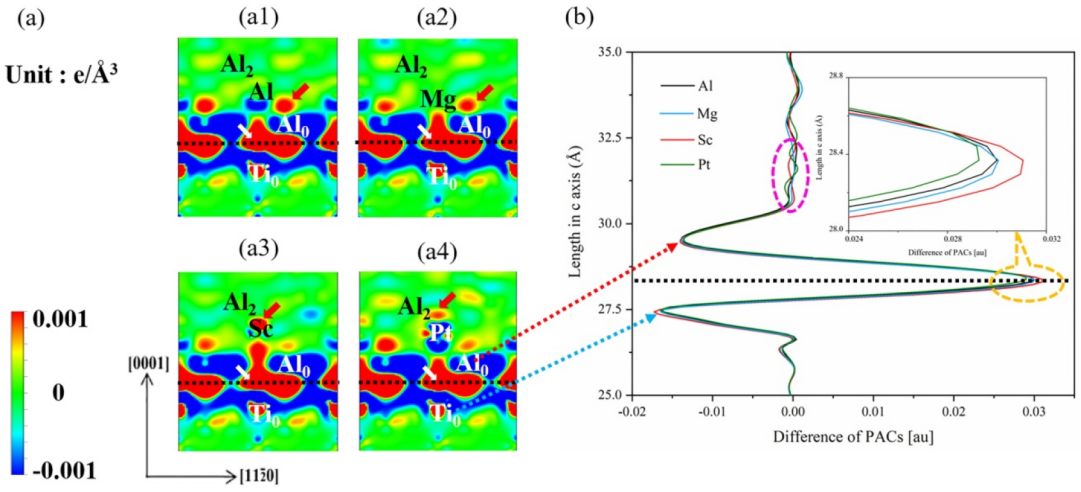

Figure 6. Charge density difference maps of the original and alloyed Ti-center Al(111)/TiB_2(0001) interfaces: (a) the (11$\bar{2}$0) plane for the interfaces; (b) the planar-averaged charge along the *c* direction for the interfaces. The dotted lines give the location of the interfaces.

https://dx.doi.org/10.1021/acs.jpcc.1c00371
J. Phys. Chem. C 2021, 125, 5937−5946

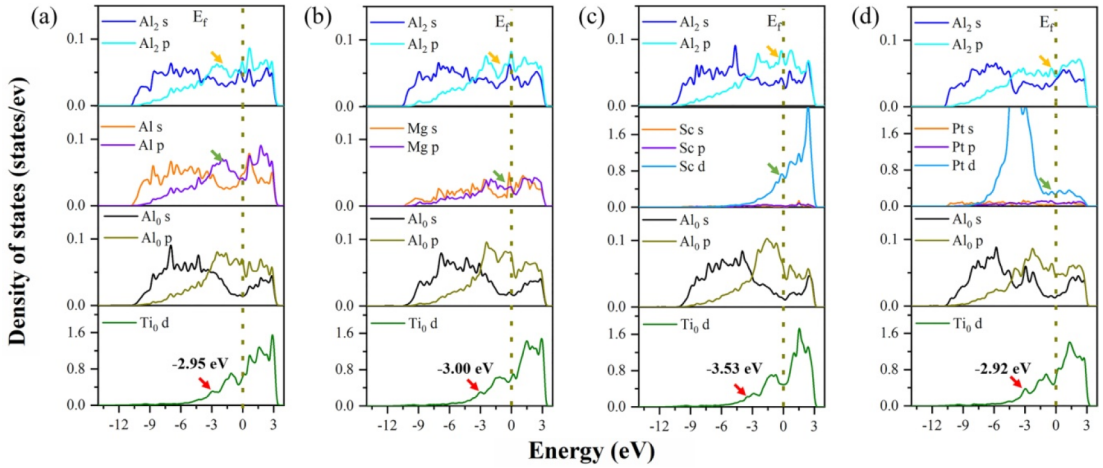

Figure 7. Layer projected density of states of the atoms at the original and alloyed Ti-center Al(111)/TiB_2(0001) interfaces. The dotted lines give the location of the Fermi level (E_f).

$$\Delta\rho = \rho_{\text{interface}} - \rho_{\text{Al-X}} - \rho_{\text{TiB}_2} \quad (8)$$

where $\rho_{\text{interface}}$, $\rho_{\text{Al-X}}$, and ρ_{TiB_2} are the total charge density of the interface system, the isolated Al or Al−X(111) slabs, and the isolated TiB_2(0001) slab in the same supercell, accordingly.

The 2D charge density differences of the $(11\bar{2}0)$ plane for the original and alloyed interfaces with Mg, Sc, and Pt atoms are plotted in Figure 6a. For the original interface, as indicated by the white arrow in Figure 6(a1), the interfacial layer has a significant charge accumulation, which originates from the charge transfer from Ti_0 to Al_0 atoms at the interface. A similar phenomenon is also found in other Al−ceramic interfaces.[57−59] Moreover, the second nearest neighbor Al atoms (i.e., Al_{i-1} layer) have some charge accumulations (indicated by the red arrow), which originate from the charge transfer between the Al and Al_0 atoms in the adjacent layer. The same phenomenon has been found in the Al(L)/TiB_2(S) interface.[60]

When the Mg adds to the interface, the charge accumulation of the interface layer in Figure 6(a2) is slightly higher than the original interface. Meanwhile, as shown by the red arrow, the charge accumulations in inner Al atoms are mainly concentrated on the Al_{i-1} layer, which is caused by charge transfer between Al_0 and Mg atoms. For the Sc-alloyed interface in Figure 6(a3), the charge accumulation on the interface layer has the highest value among all interfaces. Moreover, the charge accumulations exist in the second and third nearest neighbor Al atoms (i.e., Al_{i-1} and Al_{i-2} layers). The charge accumulation between Al_2 and Sc atoms is significantly higher than other interfaces (indicated by the red arrow), which is caused by the stronger hybridization of the Al−Sc atom. For the Pt-alloyed interface in Figure 6(a4), the addition of Pt slightly weakens the charge accumulation on the interface layer. Since Pt atoms have a large number of valence electrons on the d orbital, there is a significant charge depletion around the Pt atom, so the Al atoms in the Al_{i-1} and Al_{i-2} layers have obvious charge accumulations displayed by the red arrow.

For a more convenient comparison, the difference of planar-averaged charge (PAC)[58,61,62] along the *c* direction is shown in Figure 6b, where the positive and negative values denote the gain and loss of charges. Through the partially enlarged part in the yellow circle, the order of the intensity of charge accumulation on the interface is Sc > Mg > Al > Pt. Notably, the effects of alloying on the electronic distribution of internal Al layers (i.e., Al_{i-1} and Al_{i-2} layers) in Mg-, Sc-, and Pt-alloyed interfaces are different (indicated by a pink circle). Combined with the charge density difference map in Figure 6a, after alloying, the charge distribution changes of the inner Al layers are obviously higher than those of the interface layer.

3.4.2. Projected Density of States. According to the change density analysis, the alloying mechanisms of Mg-, Sc-, and Pt-alloyed Ti-center Al(111)/TiB_2(0001) interfaces are different. The difference mainly comes from two parts: (1) the change of the charge accumulation at the interface and (2) the change of the electron distribution of Al atoms near the interface. Therefore, to further understand the role of alloying atoms on these changes, the layer projected density of states (PDOS) of Al, Ti, and alloying atoms on these interfaces are calculated and plotted in Figure 7.

For the original interface in Figure 7a, the localized peaks of Al_0-3p and Ti_0-3d states overlap around −2.95 eV (indicated by the red arrow) and there is a pseudogap around the Fermi level (E_f), indicating the presence of Al−Ti covalent bonds across the interface. Meanwhile, the overlapping peaks of Al_0 (3p)−Al (3p) and Al (3p)−Al_2 (3p) states shown by the blue and yellow arrows describe the p−p hybridization of the Al−Al covalent bonds in the Al(111) slab. Notably, the p−p hybridizations of Al_0−Al atoms are stronger than those of Al−Al_2 atoms, which is consistent with their charge density distribution. A similar phenomenon has also been found in the Al(L)/TiB_2(S) interface by Han et al.[60]

In Figure 7b, when Mg is introduced into the interface, the Al_0-3p and Ti_0-3d electronic hybridizations are more localized in a wider energy range (from E_f to −3.00 eV) than the original interface (from E_f to −2.95 eV). That is to say, the Al_0 (3p)−Ti_0 (3d) hybridization is slightly stronger than that in the original interface. Moreover, as displayed by the blue and yellow arrows in Figure 7b, the highly localized Al_2-3p states result from the s−p hybridizations between Al_2 and Mg atoms, which facilitates the formation of Al−Mg covalent bonding in the interface.

Concerning the Sc-alloyed interface in Figure 7c, the pseudogaps at E_f and overlapping peaks of Al_0-3p and Ti_0-3d states (signposted by the red arrow) are around −3.53 eV. Compared with −2.95 eV in the original interface, it indicates the Al−Ti covalent bonding across the interface is enhanced.

https://dx.doi.org/10.1021/acs.jpcc.1c00371
J. Phys. Chem. C 2021, 125, 5937−5946

Meanwhile, the localized peaks of Al_2 (3p) and Sc (3d) states highly overlap around E_f, representing the formation of a strong Al−Sc covalent bond in the interface.

For the Pt-alloyed interface, the PDOS of atoms appears a similar phenomenon. As shown by the red arrow in Figure 7d, the localized Ti_0-3d electrons are at −2.92 eV. Referring to −2.95 eV of the original interface, it should be the reason for the slight reduction of the charge accumulation on the interface after Pt alloying. Moreover, as indicated by the blue and yellow arrows, the Pt-3d and Al_2-3p states have a larger overlap than the original interface. It indicates that the p−d hybridization of the Al−Pt covalent bonds can boost the interfacial bonding strength of the Al/TiB_2 interface.

Based on the analysis of the electron structure of the original and alloyed Ti-center Al(111)/TiB_2(0001) interfaces, the alloying mechanisms for the zero-d (i.e., Mg and Ca), low-d (i.e., Sc, Y, Zr, Ce, and Hf), and high-d (i.e., Pd, Ag, Pt, and Au) elements are different.

- For zero-d elements, the improvement of interfacial ability mainly comes from the s−-p hybridization of Al and X atoms. Thus, they have a slightly alloying effect.
- For low-d elements, the alloying atoms can not only promote the charge transfer of Al and Ti atoms at the interface but also increase the charge accumulation in the second and third nearest interface layers. Thus, the p−d hybridization of Al−X covalent bonds makes low-d elements displaying a significant alloying effect.
- For high-d elements, although the alloying slightly weakens the charge accumulation on the interface, the hybridization of interfacial atoms can compensate for it. Thus, the moderate improvement of interfacial ability mainly comes from the p−d hybridization of Al and X atoms.

Therefore, the alloying elements that can form a strong hybridization with atoms near the interface should be given priority in the future research of alloying interface design.

4. CONCLUSIONS

A large DFT database of alloying behavior at the Al(111)/TiB_2(0001) interfaces was constructed. The interfacial stability and wettability of the interfaces without or with alloying atoms have been systematically studied based on the formation energy, interface energy, and work of adhesion. The following conclusions are drawn:

(1) In the original Al(111)/TiB_2(0001) interface, the interfacial Al atoms at the two termination interfaces prefer to obey the center stacking sequence. The interfacial bonding strength of the Ti-center interface is higher than that of the B-center interface. Over most of the B chemical potential, the Ti-center interface has smaller interface energy. Therefore, the Ti-center interface has higher thermodynamic stability, so it was selected to analyze the alloying behavior of 37 elements.

(2) In the alloying interface, adding 28 of 37 elements can enhance the interfacial stability, and their optimal substitution position is mainly in the Al_{i-1} site, except for Ga (Al_i site) and Ce (Al_{i-2} site). Among them, the addition of 11 elements can further enhance the interfacial wettability. Accordingly, an alloying map containing 11 excellent elements (i.e., Mg, Ca, Ag, Ce, Au, Pd, Y, Sc, Pt, Hf, and Zr) can be obtained. These elements can effectively improve the dispersion of TiB_2 particles in Al-based composites by promoting the formation of the Al/TiB_2 interface and improving the interfacial wettability.

(3) Based on the number of valence electrons in the d orbital, these excellent elements can be divided into zero-d (Mg and Ca), low-d (Sc, Y, Zr, Ce, and Hf), and high-d (Pd, Ag, Pt, and Au) elements. Combined with the electronic structure of the alloying interface, the alloying effects are mainly influenced by the hybridization of Al and X atoms. Among the 11 elements, the p−d hybridization of low-d atoms shows a better alloying effect, the p−d hybridization of high-d atoms displays a moderate alloying effect, and the s−p hybridization of zero-d alloying atoms exhibits a weaker alloying effect.

Conclusively, alloying elements that can form strong hybridization with atoms near the interface should be given priority in the future research of alloying interface design.

■ ASSOCIATED CONTENT

Supporting Information

The Supporting Information is available free of charge at https://pubs.acs.org/doi/10.1021/acs.jpcc.1c00371.

The convergence test of the original and alloyed Al(111)/TiB_2(0001) interface models (PDF)

■ AUTHOR INFORMATION

Corresponding Authors

Mingliang Wang − *State Key Laboratory of Metal Matrix Composites, Shanghai Jiao Tong University, Shanghai 200240, China;* orcid.org/0000-0003-4866-9371; Email: mingliang_wang@sjtu.edu.cn

Hong Zhu − *School of Materials Science and Engineering, Shanghai Jiao Tong University, Shanghai 200240, China; University of Michigan - Shanghai Jiao Tong University Joint Institute, Shanghai Jiao Tong University, Shanghai 200240, China;* orcid.org/0000-0001-7919-5661; Email: hong.zhu@sjtu.edu.cn

Authors

Qian Wang − *State Key Laboratory of Metal Matrix Composites and School of Materials Science and Engineering, Shanghai Jiao Tong University, Shanghai 200240, China;* orcid.org/0000-0003-0429-8126

Yuanyuan Li − *State Key Laboratory of Metal Matrix Composites and School of Materials Science and Engineering, Shanghai Jiao Tong University, Shanghai 200240, China;* orcid.org/0000-0002-2705-8099

Siyi Chen − *State Key Laboratory of Metal Matrix Composites and School of Materials Science and Engineering, Shanghai Jiao Tong University, Shanghai 200240, China;* orcid.org/0000-0002-8812-8855

Xiaomin Liu − *School of Materials Science and Engineering, Shanghai Jiao Tong University, Shanghai 200240, China;* orcid.org/0000-0002-3436-9047

Zhe Chen − *School of Materials Science and Engineering, Shanghai Jiao Tong University, Shanghai 200240, China*

Haowei Wang − *State Key Laboratory of Metal Matrix Composites and School of Materials Science and Engineering, Shanghai Jiao Tong University, Shanghai 200240, China*

Complete contact information is available at:

https://dx.doi.org/10.1021/acs.jpcc.1c00371
J. Phys. Chem. C 2021, 125, 5937−5946

https://pubs.acs.org/10.1021/acs.jpcc.1c00371

Notes

The authors declare no competing financial interest.

■ ACKNOWLEDGMENTS

This work is sponsored by the project funded by the National Natural Science Foundation of China (Grant No. 52071207), the National Key Research and Development Program of China (Grant No. 2018YFB1106302), and the National Natural Science Foundation of China (Grant No. 51821001).

■ REFERENCES

(1) Moya, J.; Lopezesteban, S.; Pecharroman, C. The Challenge of Ceramic/metal Microcomposites and Nanocomposites. *Prog. Mater. Sci.* **2007**, *52*, 1017−1090.
(2) Kumar, N.; Gautam, G.; Gautam, R. K.; Mohan, A.; Mohan, S. Synthesis and Characterization of TiB_2 Reinforced Aluminium Matrix. Composites: A Review. *J. Inst. Eng. (India): Ser. D* **2015**, *97*, 233−253.
(3) Stefanescu, D. M.; Dhindaw, B. K.; Kacar, S. A.; Moitra, A. Behavior of Ceramic Particles at the Solid-liquid Metal Interface in Metal Matrix Composites. *Metall. Trans. A* **1988**, *19*, 2847−2855.
(4) Schaffer, P. L.; Miller, D. N.; Dahle, A. K. Crystallography of Engulfed and Pushed TiB_2 Particles in Aluminium. *Scr. Mater.* **2007**, *57*, 1129−1132.
(5) Tjong, S. C. Novel Nanoparticle-Reinforced Metal Matrix Composites with Enhanced Mechanical Properties. *Adv. Eng. Mater.* **2007**, *9*, 639−652.
(6) Chawla, N.; J, J. W.; Andres, C.; Allison, J. E. Effect of SiC Volume Fraction and Particle Size on the Fatigue Resistance of a 2080 Al/SiCp Composite. *Metall. Mater. Trans. A* **1998**, *29*, 2843−2854.
(7) Davidson, D. L. Fracture Characteristics of Al-4 Pct Mg Mechanically Alloyed with SiC. *Metall. Trans. A* **1987**, *18*, 2115−2128.
(8) Ahmad, S. N. A. S.; Hashim, J.; Ghazali, M. I. Effect of Porosity on Tensile Properties of Cast Particle Reinforced MMC. *J. Compos. Mater.* **2007**, *41*, 575−589.
(9) Tjong, S. C.; Wang, G. S. High-cycle Fatigue Properties of Al-based Composites Reinforced with In Situ TiB_2 and Al_2O_3 Particulates. *Mater. Sci. Eng., A* **2004**, *386*, 48−53.
(10) Geng, J.; Liu, G.; Wang, F.; Hong, T.; Dai, J.; Wang, M.; Chen, D.; Ma, N.; Wang, H. Microstructural Correlated Damage Mechanisms of the High-cycle Fatigued In-situ TiB_2/Al-Cu-Mg Composite. *Mater. Des.* **2017**, *135*, 423−438.
(11) Lakshmi, S.; Lu, L.; Gupta, M. J. In Situ Preparation of TiB_2 Reinforced Al-based Composites. *J. Mater. Process. Technol.* **1998**, *73*, 160−166.
(12) Emamy, M.; Mahta, M.; Rasizadeh, J. Formation of TiB_2 Particles during Dissolution of $TiAl_3$ in Al-TiB_2 Metal Matrix Composite Using an In Situ Technique. *Compos. Sci. Technol.* **2006**, *66*, 1063−1066.
(13) Han, Y.; Liu, X.; Bian, X. In Situ TiB_2 Particulate Reinforced Near Eutectic Al-Si alloy Composites. *Composites, Part A* **2002**, *33*, 439−444.
(14) Feng, C.; Froyen, L. Microstructures of In Situ Al/TiB_2 MMCs Prepared by a Casting Route. *J. Mater. Sci.* **2000**, *35*, 837−850.
(15) Geng, J.; Liu, G.; Wang, F.; Hong, T.; Xia, C.; Wang, M.; Chen, D.; Ma, N.; Wang, H. Microstructural and Mechanical Anisotropy of Extruded In-situ TiB_2/2024 Composite Plate. *Mater. Sci. Eng., A* **2017**, *687*, 131−140.
(16) Mathew, J.; Mandal, A.; Warnett, J.; Williams, M. A.; Chakraborty, M.; Srirangam, P. X-ray Tomography Studies on Porosity and Particle Size Distribution in Cast In-situ Al-Cu-TiB_2 Semi-Solid Forged Composites. *Mater. Charact.* **2016**, *118*, 57−64.
(17) Mandal, M.; Mitra, R. Effect of Pre-cold Rolling on the Evolution of Microstructure, Microtexture, and Mechanical Properties of the Mushy State Rolled In-situ Al-4.5Cu-5TiB_2 Composite. *Mater. Charact.* **2018**, *146*, 267−278.
(18) Yang, Q.; Ma, Y.; Chen, Z.; Ji, G.; Wang, M. L.; Zhong, S. Y.; Wu, Y.; Ji, V.; Wang, H. W. A New Powder Metallurgy Routine to Fabricate TiB_2/Al-Zn-Mg-Cu Nanocomposites Based on Composite Powders with Pre-embedded Nanoparticles. *Materialia* **2019**, *8*, 1004581−1004586.
(19) Youssef, Y. M.; Dashwood, R. J.; Lee, P. D. Effect of Clustering on Particle Pushing and Solidification Behaviour in TiB_2 Reinforced Aluminium PMMCs. *Composites, Part A* **2005**, *36*, 747−763.
(20) Sun, J.; Zhang, X.; Cai, Q.; Zhang, Y.; Ma, N.; Wang, H. Distribution and Engulfment Behavior of TiB_2 Particles or Clusters in Wedge-shaped Copper Casting Ingot. *Trans. Nonferrous Met. Soc. China* **2015**, *25*, 54−60.
(21) Xu, Q.; Hayes, R. W.; Hunt, W. H.; Lavernia, E. J. Mechanical Properties and Fracture Behavior of Layered 6061/SiCp Composites Produced by Spray Atomization and Co-deposition. *Acta Metall.* **1999**, *47*, 43−53.
(22) Li, X. P.; Ji, G.; Chen, Z.; Addad, A.; Wu, Y.; Wang, H. W.; Vleugels, J.; Van Humbeeck, J.; Kruth, J. P. Selective Laser Melting of Nano-TiB_2 Decorated AlSi10Mg Alloy with High Fracture Strength and Ductility. *Acta Mater.* **2017**, *129*, 183−193.
(23) Jha, A; Dometakis, C The Dispersion Mechanism of TiB_2 Ceramic Phase in Molten Aluminium and Its Alloys. *Mater. Des.* **1997**, *18*, 297−301.
(24) Xue, J.; Wang, J.; Han, Y.; Li, P.; Sun, B. Effects of CeO_2 Additive on the Microstructure and Mechanical Properties of In Situ TiB_2/Al Composite. *J. Alloys Compd.* **2011**, *509*, 1573−1578.
(25) Choudhury, S.; Aguiar, J. A.; Fluss, M. J.; Hsiung, L. L.; Misra, A.; Uberuaga, B. P. Non-uniform Solute Segregation at Semi-Coherent Metal/Oxide Interfaces. *Sci. Rep.* **2015**, *5*, 13086.
(26) Kumar, A.; Barda, H.; Klinger, L.; Finnis, M. W.; Lordi, V.; Rabkin, E.; Srolovitz, D. J. Anomalous Diffusion Along Metal/ceramic Interfaces. *Nat. Commun.* **2018**, *9*, 52511−52518.
(27) Zhang, L.; Zheng, Q.; Jiang, H.; Zhao, J. Interfacial Energy Between Al melt and TiB_2 Particles and Efficiency of TiB_2 Particles to Nucleate α-Al. *Scr. Mater.* **2019**, *160*, 25−28.
(28) Kaban, I.; Köhler, M.; Ratke, L.; Hoyer, W.; Mattern, N.; Eckert, J.; Greer, A. Interfacial Tension, Wetting and Nucleation in Al-Bi and Al-Pb Monotectic alloys. *Acta Mater.* **2011**, *59*, 6880−6889.
(29) Han, Y.; Dai, Y.; Shu, D.; Wang, J.; Sun, B. First-principles Calculations on the Stability of Al/TiB_2 Interface. *Appl. Phys. Lett.* **2006**, *89*, 1441071−1441073.
(30) Zhao, W.; Sun, Z.; Gong, S. Vacancy Mediated Alloying Strengthening Effects on γ/γ' interface of Ni-based Single Crystal Superalloys: A first-principles study. *Acta Mater.* **2017**, *135*, 25−34.
(31) Phongpreecha, T.; Nicholas, J. D.; Bieler, T. R.; Qi, Y. Computational Design of Metal Oxides to Enhance the Wetting and Adhesion of Silver-based Brazes on Yttria-stabilized-zirconia. *Acta Mater.* **2018**, *152*, 229−238.
(32) Shin, D.; Shyam, A.; Lee, S.; Yamamoto, Y.; Haynes, J. A. Solute Segregation at the Al/θ'-Al_2Cu Interface in Al-Cu alloys. *Acta Mater.* **2017**, *141*, 327−340.
(33) Deng, C.; Xu, B.; Wu, P.; Li, Q. Stability of the Al/TiB_2 Interface and Doping Effects of Mg/Si. *Appl. Surf. Sci.* **2017**, *425*, 639−645.
(34) Ma, Y.; Addad, A.; Ji, G.; Zhang, M. X.; Lefebvre, W.; Chen, Z.; Ji, V. Atomic-scale Investigation of the Interface Precipitation in a TiB_2 Nanoparticles Reinforced Al-Zn-Mg-Cu Matrix Composite. *Acta Mater.* **2020**, *185*, 287−299.
(35) Tang, Y.; Chen, Z.; Borbély, A.; Ji, G.; Zhong, S. Y.; Schryvers, D.; Ji, V.; Wang, H. W. Quantitative Study of Particle Size Distribution in an In-situ Grown Al-TiB_2 Composite by Synchrotron X-ray Diffraction and Electron Microscopy. *Mater. Charact.* **2015**, *102*, 131−136.
(36) Feynman, R. P. Forces in Molecules. *Phys. Rev.* **1939**, *56*, 340−343.
(37) Perdew, J. P.; Burke, K.; Ernzerhof, M. Generalized Gradient Approximation Made Simple. *Phys. Rev. Lett.* **1996**, *77*, 3865−3868.

(38) Kresse, G.; Joubert, D. From Ultrasoft Pseudopotentials to the Projector Augmented-wave Method. *Phys. Rev. B: Condens. Matter Mater. Phys.* **1999**, *59*, 1758−1775.
(39) Li, Y. F.; Xiao, B.; Wang, G. L.; Sun, L.; Zheng, Q. L.; Liu, Z. W.; Gao, Y. M. Revealing the Novel Fracture Mechanism of the Interfaces of TiB_2/Fe Composite from a First principles Investigation. *Acta Mater.* **2018**, *156*, 228−244.
(40) Sun, J. P.; Dai, J.; Song, Y.; Wang, Y.; Yang, R. Affinity of the Interface between Hydroxyapatite (0001) and Titanium (0001) Surfaces: A First-Principles Investigation. *ACS Appl. Mater. Interfaces* **2014**, *6*, 20738−20751.
(41) Gao, B.; Jalem, R.; Tateyama, Y. Surface-Dependent Stability of the Interface between Garnet $Li_7La_3Zr_2O_{12}$ and the Li Metal in the All-Solid-State Battery from First-Principles Calculations. *ACS Appl. Mater. Interfaces* **2020**, *12*, 16350−16358.
(42) Le, H.L. T.; Goniakowski, J.; Noguera, C.; Koltsov, A.; Mataigne, J.-M. First-Principles Study on the Effect of Pure and Oxidized Transition-Metal Buffers on Adhesion at the Alumina/Zinc Interface. *J. Phys. Chem. C* **2016**, *120*, 9836−9844.
(43) Wang, X. G.; Weiss, W.; Shaikhutdinov, S. K.; Ritter, M.; Petersen, M.; Wagner, F.; Schlögl, R.; Scheffler, M. The Hematite (α-Fe_2O_3)(0001) Surface: Evidence for Domains of Distinct Chemistry. *Phys. Rev. Lett.* **1998**, *81*, 1038.
(44) Zhang, W.; Smith, J. Nonstoichiometric Interfaces and Al_2O_3 Adhesion with Al and Ag. *Phys. Rev. Lett.* **2000**, *85*, 3225.
(45) Zhang, X.; Wu, X.; Hou, C.; Li, X.; Liu, C. S. First-principles Calculations on Interface Stability and Migration of H and He in W-ZrC Interfaces. *Appl. Surf. Sci.* **2020**, *499*, 143995.
(46) Gao, L.; Li, K.; Ni, S.; Du, Y.; Song, M. The Growth Mechanisms of θ' Precipitate Phase in an Al-Cu Alloy During Aging Treatment. *J. Mater. Sci. Technol.* **2021**, *61*, 25−32.
(47) Biswas, A.; Siegel, D. J.; Wolverton, C.; Seidman, D. N. Precipitates in Al-Cu Alloys Revisited: Atom-probe Tomographic Experiments and First-principles Calculations of Compositional Evolution and Interfacial Segregation. *Acta Mater.* **2011**, *59*, 6187−6204.
(48) Zhang, C.; Jiang, Y.; Cao, F.; Hu, T.; Wang, Y.; Yin, D. Formation of Coherent, Core-shelled Nano-particles in Dilute Al-Sc-Zr Alloys from the First-principles. *J. Mater. Sci. Technol.* **2019**, *35*, 930−938.
(49) Xue, J.; Han, Y. F.; Lei, J. B.; Wang, J.; Sun, B. D. CeO_2 Induced Dispersive Distribution of TiB_2 Particles in In situTiB_2/Al Composite. *Mater. Sci. Technol.* **2014**, *30*, 871−875.
(50) Mahjoub, R.; Laws, K. J.; Stanford, N.; Ferry, M. General Trends Between Solute Segregation Tendency and Grain Boundary Character in Aluminum - An ab Inito Study. *Acta Mater.* **2018**, *158*, 257−268.
(51) Saiz, E.; Cannon, R. M.; Tomsia, A. P. High-Temperature Wetting and the Work of Adhesion in Metal/Oxide Systems. *Annu. Rev. Mater. Res.* **2008**, *38*, 197−226.
(52) Zhang, X.; Xu, P.; Zhang, M.; Liu, G.; Xu, Z.; Yang, J.; Shao, H.; Qiao, G. Improving the Wettability of Ag/ZrB_2 System by Ti, Zr and Hf Addition: An Insight from First-principle Calculations. *Appl. Surf. Sci.* **2020**, *517*, 146201.
(53) Sun, J.; Wang, X.; Guo, L.; Zhang, X.; Wang, H. Synthesis of Nanoscale Spherical TiB_2 Particles in Al Matrix by Regulating Sc Contents. *J. Mater. Res.* **2019**, *34*, 1258−1265.
(54) Zhang, X.; Sun, J.; Wang, W.; Zhang, Y.; Ma, N. Improvement of Yttrium on the Hot Tearing Susceptibility of 6TiB_2/Al-5Cu Composite. *J. Rare Earths* **2015**, *33*, 1335−1340.
(55) Wang, S.; Zhang, C.; Li, X.; Huang, H.; Wang, J. First-principle Investigation on the Interfacial Structure Evolution of the $\delta'/\theta'/\delta'$ Composite Precipitates in Al-Cu-Li Alloys. *J. Mater. Sci. Technol.* **2020**, *58*, 205−214.
(56) Wang, M.; Zhong, J. Q.; Stacchiola, D. J.; Boscoboinik, J. A.; Lu, D. First-Principles Study of Interface Structures and Charge Rearrangement at the Aluminosilicate/Ru(0001) Heterojunction. *J. Phys. Chem. C* **2019**, *123*, 7731−7739.
(57) Liu, L. M.; Wang, S. Q.; Ye, H. Q. First-Principles Study of Polar Al/TiN(111) Interfaces. *Acta Mater.* **2004**, *52*, 3681−3688.
(58) Siegel, D. J.; Hector, L. G.; Adams, J. B. Adhesion, Stability, and Bonding at Metal/metal-Carbide Interfaces: Al/WC. *Phys. Rev. B* **2002**, *498*, 321−336.
(59) Luo, K.; Deng, Q.; Zha, X.; Huang, Q.; Francisco, J. S.; Yu, X.; Qiao, Y.; He, J.; Du, S. J. M. P. Electronic Structures and Mechanical Properties of Al(111)/ZrB_2(0001) Heterojunctions from First-principles Calculation. *Mol. Phys.* **2015**, *113*, 1794−1801.
(60) Zhang, H. L.; Han, Y. F.; Dai, Y. B.; Lu, S. S.; Wang, J.; Zhang, J.; Shu, D.; Sun, B. D. An Ab Initio Study on the Electronic Structures of the Solid/liquid Interface Between TiB_2 (0001) Surface and Al Melts. *J. Alloys Compd.* **2014**, *615*, 863−867.
(61) Chen, Y.; Dai, J.; Song, Y. Stability and Hydrogen Adsorption Properties of Mg/Mg_2Ni Interface: A First Principles Study. *Int. J. Hydrogen Energy* **2018**, *43*, 16598−16608.
(62) Sun, J. P.; Song, Y. Strengthening Adhesion of the Hydroxyapatite and Titanium Interface by Substituting Silver and Zinc: A First Principles Investigation. *ACS Appl. Nano Mater.* **2018**, *1*, 4940−4954.

https://dx.doi.org/10.1021/acs.jpcc.1c00371
J. Phys. Chem. C 2021, 125, 5937−5946